# Temperature dependence of THz generation efficiency, THz refractive index, and THz absorption in lithium-niobate around 275 GHz

UMIT DEMIRBAS,[1,4,5] CHRISTIAN RENTSCHLER,[1,2,6] ZHELIN ZHANG[1,7], MIKHAIL PERGAMENT,[1] NICHOLAS H. MATLIS,[1] AND FRANZ X. KÄRTNER,[1,2,3,*]

[1]*Center for Free-Electron Laser Science CFEL, Deutsches Elektronen-Synchrotron DESY, Notkestr. 85, 22607 Hamburg, Germany*
[2]*Physics Department, University of Hamburg, Luruper Chaussee 149, 22761 Hamburg, Germany*
[3]*The Hamburg Centre for Ultrafast Imaging, Luruper Chaussee 149, 22761 Hamburg, Germany*
[4]*Paul Scherrer Institut, CH-5232 Villigen PSI, Switzerland*
[5]*Antalya Bilim University, 07190 Dosemealti, Antalya, Turkey*
[6]*Max Planck School of Photonics, Hans-Knöll-Straße 1, 07745 Jena, Germany*
[7]*Tsung-Dao Lee Institute, Shanghai Jiao Tong University, Shanghai 200240, China*
*franz.kaertner@desy.de

**Abstract:** We used pulse trains with 800-fs long pulses and adjustable time delay to investigate the temperature dependence of THz generation in a periodically pooled lithium niobate (PPLN) crystal with a poling period of 400 μm. By adjusting the PPLN temperature (78-350 K), multicycle, narrowband (sub-10 GHz) THz pulses with tunable central frequency in the 253-287 GHz range were obtained. Internal conversion efficiency values up to 0.45% were demonstrated at a peak fluence value of 150 mJ/cm$^2$ at 78 K. Via scanning the incident pulse-train frequency, we measured the frequency response of the crystal at different temperatures, which enabled us to determine the temperature dependence of the refractive index and thermo-optic coefficient of the PPLN crystal around 275 GHz with very high precision. We further studied the variation of THz generation efficiency with temperature in detail to understand the temperature dependence of THz absorption in PPLN material. Here, we observed that it is difficult to isolate the temperature dependence of absorption with high accuracy from the THz efficiency data, as the efficiency depends on many other factors that could also be temperature-dependent. Overall, the results presented in this manuscript demonstrate the capability of the tunable-frequency pulse-train excitation approach in mapping fundamental properties of nonlinear crystals at relatively low THz frequencies, where other characterization methods, such as THz time-domain spectroscopy, have difficulties.

## 1. Introduction

High-energy and high-field table-top THz sources are attractive for many applications, including spectroscopy, microscopy, imaging, metrology, communications, and medical diagnostics/treatment [1–3]. Optical rectification (OR) of ultrashort laser pulses is a well-established technique to generate (i) single-cycle THz pulses with broad spectra and high peak field or (ii) narrow-band and multicycle (MC) THz pulses with ample spectral brightness [4]. So far, most of the work with ultrashort laser-based THz sources has focused on generating single-cycle THz pulses [5–9] due to their high electric field strength and broad bandwidth. However, over the last few years, there has been a growing interest in the development of MC THz pulses as well [10–18] for applications such as particle acceleration [10], spectroscopy [19,20], and coherent control of matter [21] where resonant excitation via tunable narrowband sources has advantages over broadband excitation.

A well-known method for generating narrowband multi-cycle THz sources is to exploit the velocity mismatch between the optical and THz pulses in poled nonlinear crystals such as PPLN [4]. Via quasi-phase-matching (QPM) in these structures, a THz waveform that corresponds to the domain structure of the poled nonlinear crystal is obtained [22]. Ignoring THz absorption in the nonlinear crystal, excitation of these periodically poled crystals with a single ultrashort pulse generates an MC THz pulse with N cycles, where N is the number of poling periods in the crystal. MC THz pulses could also be obtained via spatial, temporal, and/or spectral shaping of the pump pulses using phase masks [23], transient gratings [24], spatial light modulators [25], chirped pulse-beating [14], two-line seeding [11], and Michelson interferometer-based pulse dividers [26]. While applying these pump pulse shaping techniques often, one could still use periodically poled crystals (such as PPLN) as the nonlinear medium. In such a case, the pump source and the periodically poled crystal structure contribute to the narrowing of the multi-cycle THz wave, and one can achieve bandwidths narrower than what could be achieved while employing these techniques separately. In our recent work [26], we have used a train of sub-ps optical pulses (generated via a pulse divider setup) to excite PPLN in cryogenic operation, and we have shown that this system (i) enables precise parameter control of the generated MC THz pulse, (ii) allows mapping of the key properties of the nonlinear medium used with unprecedented precision, and (iii) empowers generation of THz spectra with record spectral brightness levels. In [26], we also have provided a detailed analytical model that can be used to understand the role of periodically-poled crystals and the pulse train in the MC THz generation process.

In this follow-up study, we demonstrate frequency mapping characteristics of the pulse train in more detail by measuring the temperature dependence of important optical properties of PPLN, such as refractive index, thermo-optic coefficient, and absorption coefficient around a central THz frequency of 275 GHz. This is the frequency range where other material characterization methods, such as THz time-domain spectroscopy, have difficulties providing the required precision [27–30]. In our experiments, using the pulse-train excitation as a tool, we utilized the THz generation process itself to acquire knowledge on the nonlinear crystal used for THz generation, enabling an in-situ measurement under actual experimental conditions. Via scanning the periodicity of the pulse train used for excitation, we have first mapped the frequency response of a PPLN crystal with a poling period of 400 μm as a function of temperature between 78 K and 350 K. Using this data, we have then determined the temperature dependence of the refractive index of the PPLN material with unprecedented precision. Later, the temperature dependence of the THz generation efficiency was also explored in detail to study the variation of THz absorption of the PPLN crystal with temperature. Here, we see that, as parameters such as the effective nonlinear optical coefficient are also temperature dependent, it is challenging to isolate the temperature dependence of absorption accurately from the THz efficiency data. Overall, as an example, this study reports the characterization of PPLN crystal around a center frequency of 275 GHz, but the technique employed is quite general and could be applied to both other frequency ranges and nonlinear crystals.

## 2. Experimental Setup

A home-build laser system consisting of a seeder, regenerative amplifier, and a multi-pass amplifier was developed as the pump source for THz generation (Fig. 1). This system has been recently introduced in detail in [26], so here our discussion will be brief. The Yb-fiber-based seeder system, which includes a mode-locked oscillator and 2 fiber-based amplifiers, provides chirped (~ns) pulses with around 400 mW average power at a repetition rate of 40 MHz. The optical spectra of the pulses from the seeder have an FWHM of about 10 nm centered around 1034 nm. A pair of transmission gratings is used as a “pre-compressor” to compress the pulses to around 3 ps. This quasi-compression before the regen is necessary to

accurately generate and correctly characterize the pulse train in the pulse divider setup. The pulse divider setup consists of eight polarization-based Michelson interferometers (pulse divider stages). It enables the generation of a pulse train with an adjustable pulse number (from 1 to $2^8$ : 256). Figure 2 shows the first four stages of the pulse divider setup.

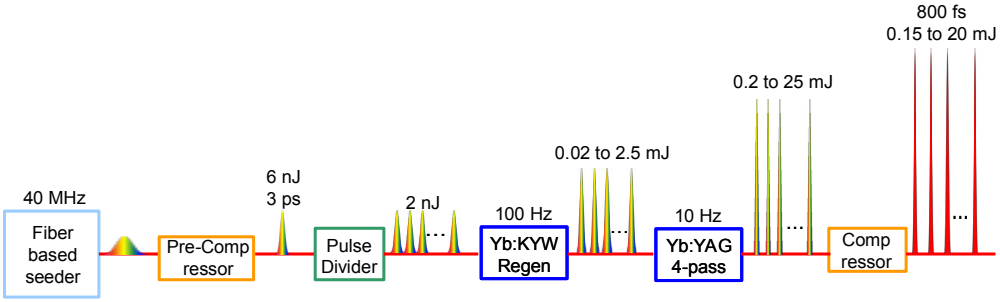


Fig. 1. Schematic of the home-built laser source developed for THz generation experiments. The system produces a train of 800 fs pulses with burst lengths up to a nanosecond and burst energies up to 20 mJ.

In each divider stage, we split the incident beam into two using a halfwave plate (HWP, λ/2) and a polarizing beam splitter (PBS, polarizer) cube. The beams recombine on the PBS after inducing a 90-degree polarization rotation upon double-pass through quarter-wave plates (QWP, λ/4). The distance between the pulses could be freely adjusted by controlling the length of the interferometer arms (the distances in Fig. 2 is an example of a pulse divider frequency setting of 300 GHz).

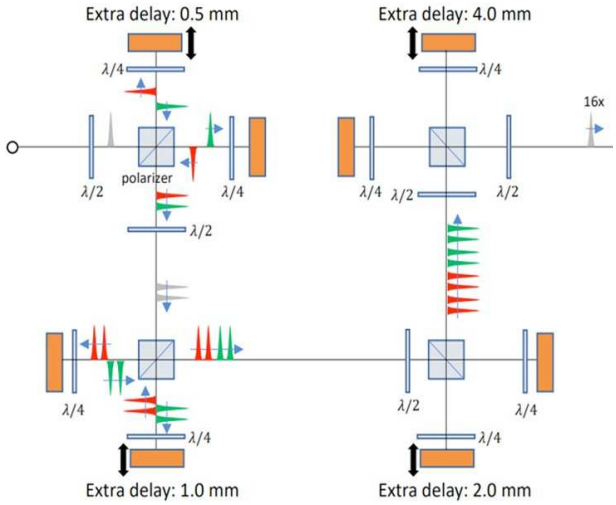


Fig. 2. Schematic layout of the first four stages of the pulse divider setup used to generate the pulse train. The first 4 stages shown here create a pulse train with (2^4) 16 pulses. When followed by a similar setup consisting of 4 more stages, the system could generate a pulse train with up to (16*16) 256 pulses.

The nJ pulse energies of the pulse train (pulse burst) are then amplified in a room-temperature Yb:KYW regenerative amplifier up to 2.5 mJ energy [31]. A short pass filter placed before the regen (not shown in Fig. 1) is used to cut the seeder spectrum above 1035 nm and reduce the seeder bandwidth to ~5 nm for stable operation of the entire amplifier system. This enabled the regen to operate around a central wavelength of 1030 nm, and due to gain narrowing, the spectral width of regen output was reduced to around 3 nm. The regen output is then further scaled up to 25 mJ in a room-temperature 4-pass Yb:YAG amplifier.

Due to further gain narrowing in the Yb:YAG crystal, the final spectral width of the pulses is reduced to 1.9 nm. The pulses could be compressed down to 800 fs (estimated time-bandwidth product is around ~0.4 assuming a $Sech^2$ pulse shape). Due to thermal effects, the room-temperature regenerative amplifier is operated at 100 Hz, and the 4-pass Yb: YAG amplifier is operated at 10 Hz, which is the repetition rate used in these initial experiments. We are developing a cryogenic Yb: YLF-based amplifier producing 100 mJ level sub-ps pulses at a 1 kHz repetition rate [32,33], and upgrading the setup to this system will further increase the SNR of our data and reduce data-taking times in future studies.

As a side note, during these experiments, we realized the onset of self-focusing during the amplification process, especially when the amplifier is seeded with a pulse burst containing only a few pulses. This is expected, as in our system, the number of pulses in the pulse train determines the burst width (stretching amount). For example, for a pulse train consisting of only 2 pulses, the pulse burst width is only around 5 ps. When seeding the amplifier with such a short pulse, nonlinear effects are unavoidable. To minimize nonlinear effects, such as self-phase modulation during amplification, we have limited the output energies to around 0.2 mJ while only amplifying a pulse burst consisting of 2 pulses. On the contrary, for a pulse train with 256 pulses, the burst width is around 950 ps, and the pulse burst could safely be amplified to 25 mJ level (note that the energy of each pulse within the burst stays below ~ 0.1 mJ). For burst lengths in between, the amplifier energy is adjusted accordingly. In future studies, one can move the pulse-divider stage after the main amplifier to achieve similar energy levels for different burst lengths. As a drawback, this will require using large beam size and thin optics in the pulse divider setup to minimize self-phase modulation and laser-induced damage. Also, the pulse divider output contains both s and p-polarized light, and hence, half of the amplifier output will then be unusable for THz experiments (unless one uses two separate THz generation setups).

For THz generation experiments, the compressed pulse train is then sent into a commercial PPLN crystal with a poling period of 400 μm (Fig. 3). The PPLN crystal had an aperture of 4x4 $mm^2$ and a length of 20 mm (the 4 mm thickness is currently the largest thickness that could be commercially obtained). For the 20 mm length, the crystal contains (20/0.4) around 50 poling periods ($N_{PPLN}$ as defined in [26]). The lithium niobate sample used in this study was grown from a congruently melted composition and doped with 5% magnesium oxide (MgO) to minimize green-induced infrared absorption and photorefractive beam distortions (in literature these crystals are named as MCLN, C indicating the congruent growth, and M indicating MgO doping). Both surfaces of the PPLN sample were AR-coated for the pump wavelength. The crystal was placed inside a dewar and cooled to cryogenic temperature (78 K) by boiling liquid nitrogen. The dewar cold head also contained a resistive heater to adjust the crystal temperature. The slow heating cycle (~5 hours) of the dewar and the resistive heater in the cold head are used to tune the temperature of the PPLN crystal over the 78-350 K range.

Using a telescope consisting of lenses with focal lengths of 10 cm and -5 cm (f1 and f2 in Fig. 3), the $1/e^2$ diameter of the pump beam on the crystal is adjusted to a beam size of 3 mm on the crystal (monitored with a camera using a beam sampler). The 4x4 $mm^2$ aperture of the PPLN crystal enabled a throughput of around 97% through the crystal aperture for this beam size. Note that using smaller beam sizes reduces THz efficiencies due to undesired effects such as self-focusing in LN (a topic that will be discussed in detail in a follow-up study) [34]. Hence, the pump beam diameter on the PPLN is kept at 3 mm despite the minor aperture effects. The THz radiation is generated collinearly with the laser beam and collected and focused onto a THz detector (Gentec SDX-1152 with a 9 mm diameter active area) by a pair of 10 cm focal length, 2-inch off-axis parabolas (OAPs) with a protected gold coating. The pump beam and the THz radiation polarization are parallel to the extraordinary axis of the lithium niobate crystal (all polarized along the z-axis to benefit from the large $d_{33}$ coefficient of LN). The output of the Gentec detector is monitored with an oscilloscope. The voltage

reading in the scope is converted into a THz energy with a conversion factor of (74 ± 3) mV/μJ (calibration of the detector is performed in-house by comparing its reading with a calibrated sensor from Lasertechnik GmbH) [6,35]. A 1 cm thick Teflon slab was inserted between the two OAP mirrors to entirely block the remaining pump beam (the filter had a transmission of 83% around 300 GHz [26]). The first OAP mirror had a 3 mm wide through-hole to allow passage of most of the pump beam (MPD249H-M01), which is then used to characterize the changes in the spectral content of the transmitted pump beam. The second OAP mirror also contained a through-hole to allow passage of a portion of the compressed seed beam for electro-optic sampling of the THz field (not shown in Fig. 3). For the EO sampling experiments, a 0.5 mm thick 10x10 $mm^2$ aperture <110> cut ZnTe crystal is employed.

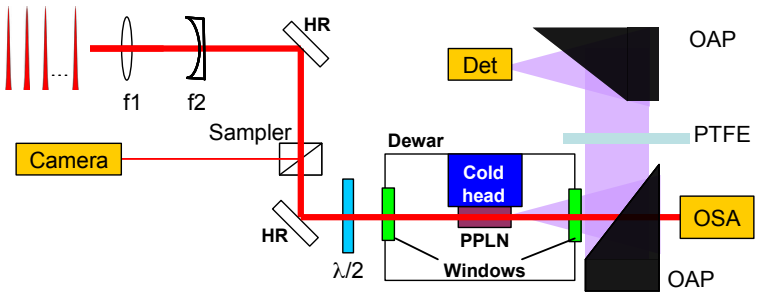


Fig. 3. Schematic layout of the THz generation setup used in the experiments. OAP: Off-axis parabola, OSA: Optical spectrometer, Det: THz energy meter, HR: Pump high-reflector.

We performed two sets of experiments in this study. In the first experimental campaign, the energy of the pump pulse burst is kept constant, and the period of the pulse train is scanned to measure THz energy as a function of pulse train frequency. This measurement enabled mapping of the frequency response of the crystal. The measurement has been performed for PPLN crystal temperatures between 78 K and 350 K with about 5 K temperature increments, and the data is repeated 3 times in different days to confirm the results. In the second set of experiments, the pulse train frequency is kept constant (adjusted to the resonance frequency of the PPLN crystal that is now known), and the incident pulse burst energy is scanned to measure the variation of generated THz energy with input pulse energy (in this paper with the incident energy we mean the total energy of the pulses within the burst). This measurement has been performed for different crystal temperatures between 78-350 K with about 10 K temperature increments, and the data is repeated two times to confirm the validity of the results. Throughout the study, to avoid optically induced damage to the PPLN crystal, the incident pulse train peak fluence was limited to 150 $mJ/cm^2$ at 78 K and 500 $mJ/cm^2$ at room temperature. The first set of data is used to determine the THz resonance peak of the PPLN crystal at different temperatures, which is used to estimate the temperature dependence of the refractive index of the PPLN crystal in the THz frequency range. The second set of data (along with the first set) is used to study the temperature dependence of THz efficiency, which is used to study the temperature dependence of THz absorption in the PPLN crystal.

In our analysis, the “internal” conversion efficiency, i.e., the ratio of THz to optical pulse energy within the crystal, is used to quantify the THz yield. Usage of this metric allows evaluation of the performance of the THz generation process decoupled from practical issues associated with output coupling and transport of THz radiation. For this purpose, in our setup, we have considered losses due to the dewar exit window (fused silica: 35%), 1 cm thick

Teflon filter (17%), and reflection loss on the exit surface of the PPLN crystal (43% at 78 K, and 45.7% at 350K due to the change in refractive index values with temperature). Hence, we estimated a total loss level of around 70% for our setup.

## 3. Results and Discussions

### *3.1 Calibration of pulse train frequency and confirmation with EO sampling*

As a starting point, we first validated the correct frequency mapping capability of the pulse train. This is required as the accurate mapping capability of the pulse train depends on the correct adjustment of distances in the pulse train divider setup interferometer arms. For high-precision adjustment of the lengths of the interferometer arms (with sub-10 µm precision), we have investigated several methods such as spectral interference, spatial interference, autocorrelation, and THz efficiency scan. Among the methods used, we have seen that autocorrelation is the most straightforward approach while adjusting the distances of the first five stages.

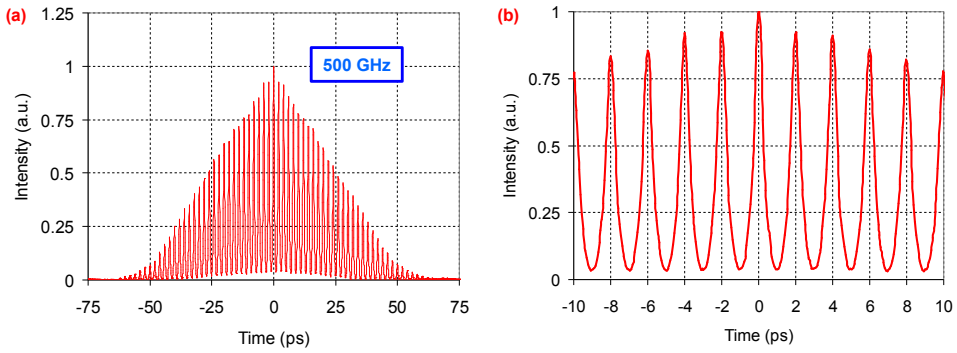


Fig. 4. (a) Autocorrelation of pulse train from the first five stages (32 pulses) for a set frequency of 500 GHz, (b) Zoomed-in autocorrelation trace showing a pulse separation of 2 ps that is required for resonant excitation at 500 GHz.

For example, Fig. 4 (a) shows the recorded autocorrelation of the pulse train for a central frequency of 500 GHz. In this example, we see the pulses from the first five divider stages, where the pulse burst has 32 pulses, and the autocorrelation trace shows 63 peaks. The distance between the peaks is 2 ps, as shown in Fig. 4 (b). The resolution of this method in the time domain is limited by the pulse width of the pulses in the pulse bunch. For this test, we readjusted the pre-compressor to compress the seeder pulses to around 300 fs, which provided us with a pulse timing adjustment error of about ±10 fs, which corresponds to a distance adjustment error of around ±3 µm. In Fig. 4, we see the autocorrelation of all the 32 pulses. It is essential to state that one needs to confirm the calibration of the autocorrelator for this method to work correctly, as our device was initially measuring the pulses 5.4% shorter, and we have recalibrated our autocorrelator for the proper setting of the distances.

The scanning range of the autocorrelator at hand in our experiments was limited to 150 ps, and hence, for the precise setting of the distances in our 6$^{th}$ and 7$^{th}$ stages, we have looked at the variation of THz efficiency around the resonance of the crystal, by scanning each stage separately and looking at the THz yield variation. For example, Fig. 5 shows a frequency scan for the first seven stages independently. As we can see, the THz efficiency is sensitive to the correct adjustment of frequency/delay of stages, and this can be used to optimize the arm lengths. We have used this method to fine-tune all stages' distances to obtain a sharp resonance signal.

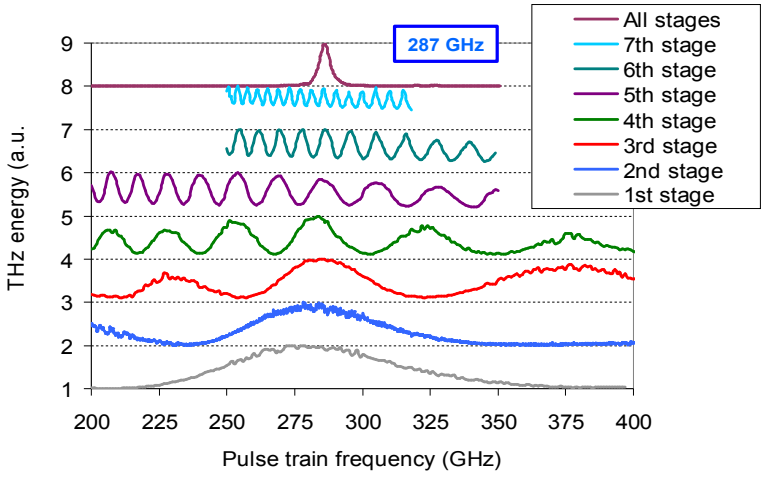


Fig. 5. Optimization of the delay stage arm positions by measuring the effect of stage distance on THz efficiency. Once all the stages are positioned correctly, the pulse train's frequency scan can map the nonlinear crystal's frequency response with high precision.

Once the interferometer distances were adjusted as described above, we tested our system's frequency scan capability. For example, in Fig. 6 (a), we show the measured pulse train frequency scan data of the 400 µm QPM period crystal along with other PPLN samples with QPM periods of 330 µm and 600 µm at 78 K and at room temperature. The data is taken using a pulse train with 128 pulses. We see that a frequency scan with the pulse train source enables a quick but detailed measurement of the frequency response of each crystal. These measurements currently take around ~10 minutes, but we hope to reduce these scanning times to below a minute in future studies once we employ the 1 kHz Yb:YLF laser in our THz system. Hence, this frequency response measurement-based system could be used to quickly identify nonlinear crystals.

An alternative method of frequency response measurements is the well-known electro-optic (EO) sampling technique. To independently confirm the calibration of our pulse train frequency scans, we have performed EO sampling with 400 µm QPM period PPLN crystals at 78 K. Fig. 6 (b) shows the calculated frequency spectrum of the generated THz field from the measured EO sampling data along with the frequency scan approach measurement (details of EO sampling data is shown in Fig. 6 (c-d)). As we can see from Fig. 6 (b), at 78 K, the PPLN crystal has a peak THz response around 286.5 GHz, and the bandwidth (full width at half maximum, FWHM) of the response curve is around 5 GHz. We can see that within experimental errors, the EO sampling data match the pulse train frequency scan measurement quite well, and both curves are close to the calculated analytical curve (for the analytical curve we have assumed zero THz absorption). It is instructive to look at the bandwidth obtained here in a little more detail, which is 5 GHz around a central frequency of 286.5 GHz. This corresponds to a bandwidth-to-central frequency percentage of 1.75% [26]. We know that, for small absorption values, the bandwidth of the THz can be estimated as $0.89/N_{PPLN}$, and for our case, the number of poling periods in our 2 cm long crystal is around 50. So, a simple analytical estimation for the bandwidth is 1.8%, which is in very good agreement with what has been measured. The good fit between the analytical curve and measurements also confirms this analysis.

In closing this subsection, it is important to note that the EO sampling data is taken in around 10 hours due to the low signal-to-noise ratio and low repetition rate of the pump

source. In comparison, the pulse train frequency data provides similar information in a much shorter time scale (frequency scan data is taken between 250 and 325 GHz with a step size of 0.25 GHz, and the whole data could be taken in 5-10 minutes). As the frequency scan characterization is relatively fast, this reduces the risk of damage to the crystal: in one of our long-term (10 hours) EO sampling measurements, we damaged one of our crystals at a peak fluence of 200 mJ/cm$^2$. Moreover, in long EO sampling measurements, the changing parameters of the laser or other factors could induce noise in the data. In contrast, these factors could be kept more constant in a short frequency scan measurement with the pulse train.

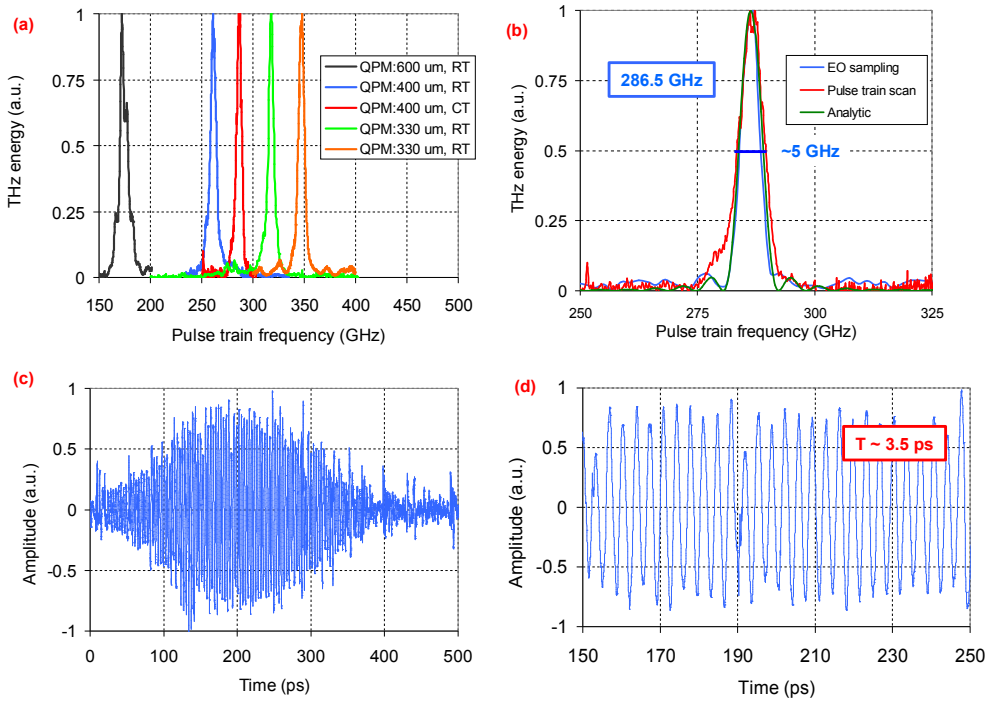


Fig. 6. (a) Frequency response of the PPLN crystals with QPM periods of 600 µm, 400 µm, and 330 µm at cryogenic temperature (CT: 78 K) and room temperatures (RT: ~295 K). The measurement has been performed using the pulse train frequency scan technique. (b) Measured frequency response of the PPLN crystal at 78 K. For comparison, the frequency spectra measured using electro-optic sampling and pulse train frequency scan are shown along with the calculated analytical frequency response curve. (c) Measured electro-optic sampling trace of the long THz pulse generated by the pulse train. The data is collected at 78 K while exciting the crystal with 64 pulses. The THz pulse contains around 100 cycles. (d) The zoomed-in EO-sampling trace between 150 and 250 ps, showing a periodicity of about 3.5 ps.

## 3.2 Temperature dependence of frequency response of PPLN and estimation of THz refractive index and thermo-optic coefficient

After confirming the validity of the pulse train frequency scan approach, as described in the earlier section, we have then measured the frequency response of the PPLN crystal using the pulse train as a function of temperature for temperatures between 78 K and 350 K. Figure 7 provides measured frequency response curves at selected temperatures. As we can see from Fig. 8, the peak response of the crystal shifts from around 286.5 GHz at 78 K to 253 GHz at 350 K. We have repeated this experiment three times on different days, and the measurements

data confirmed each other quite well (Data 1 to 3 in Fig. 8). The following simple analytic formula could be used to model the measured temperature dependence of the resonance THz frequency ($f_{THz}$) for the 400 μm QPM MCLN crystal used in this study:

$$f_{THz}(T) = 290.55 - 4.1 \cdot 10^{-2} T - 1.9 \cdot 10^{-4} T^2 \qquad (1)$$

In Eq. 1, $f_{THz}$ has the units of GHz, and T is the temperature in the units of Kelvin. Note that we have used step sizes of 0.25-0.5 GHz in our measurements, hence, the error bar due to the frequency resolution limit we have chosen is around ±0.1-0.2%.

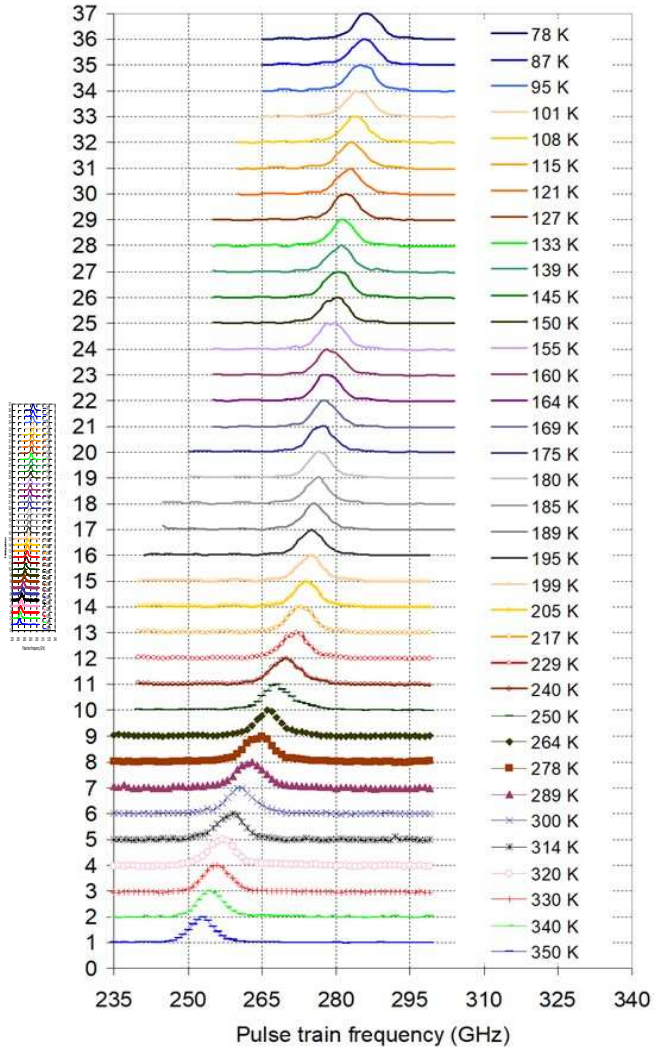


Fig. 7. Measured frequency response of the PPLN crystal as a function of temperature between 78 K and 350 K. The data is taken with the 2 cm long PPLN crystal with a QPM period of 400 μm at an incident energy of 4 mJ, a pump diameter of 3 mm, and a pulse burst of 64 pulses.

There is little detailed report for temperature tuning of the THz frequency for PPLN in literature to directly compare our data. In general, the measured trend in this study is quite similar to earlier reported frequency tuning curves at higher (>1 THz) frequencies [36]. As a side note, as one increases the temperature due to increased absorption losses of the PPLN crystal, the obtainable THz energies decrease significantly, which is also observed during these frequency scans, but in Fig. 7, we have chosen to show the curves on a normalized scale, as we want to focus on variation of resonance frequency peaks with temperature. For completeness, we show sample frequency scan curves taken at selected temperatures in Fig. 9, where we normalized all the curves to the maximum energy level obtained at 78 K. The variation of THz efficiency/yield with temperature will be discussed in detail in the next section.

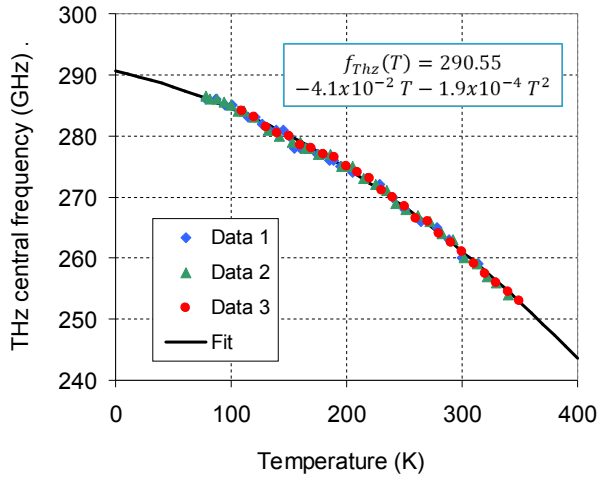


Fig. 8. Measured variation of THz central frequency as a function of PPLN crystal temperature. The solid curve is an analytical fit to the measured data. A 5% MgO-doped congruently grown lithium niobate (MCLN) with a QPM period of 400 μm was used in the experiments.

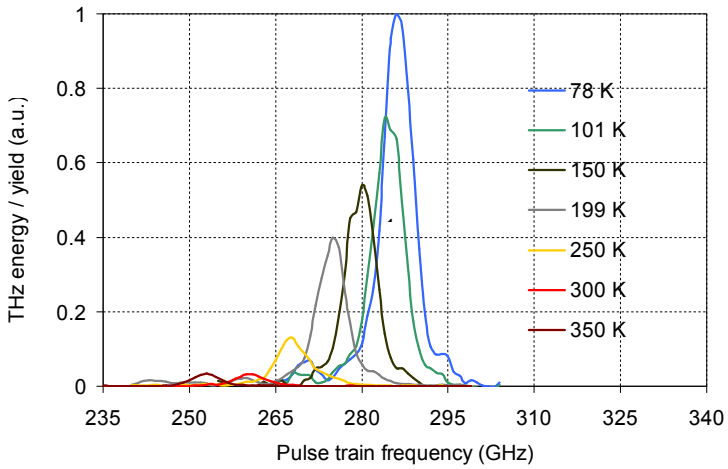


Fig. 9. Measured frequency scan curves of PPLN at selected temperature between 78 K and 350 K. The data is normalized to the maximum energy obtained at 78 K and clearly shows the

effect of absorption in reducing THz yield. The data is taken with the 2 cm long PPLN crystal with a QPM period of 400 μm at an incident energy of 4 mJ, a pump diameter of 3 mm, and a pulse burst of 64 pulses.

The measured variation of the THz resonance frequency with temperature could then be used to calculate the refractive index of the THz wave in PPLN as a function of temperature (for the extraordinary axis). It is well-known that, for the forward propagating THz wave, the phase matching condition supports a THz wave with a central frequency ($f_{THz}$) of [4]:

$$f_{THz} = \frac{c}{\Lambda(\Delta n)} = \frac{c}{\Lambda\left(n_{THz} - n_{gr}^{opt}\right)}. \quad (2)$$

Here, c is the speed of light, $\Lambda$ is the QPM orientation reversal period (400 μm in our case), $n_{gr}^{opt}$ is the optical group velocity refractive index, and $n_{THz}$ is the phase refractive index for the THz wave, and $\Delta n$ is the difference between the THz-phase and optical group indices. Measured data in Fig. 8 and Eq. (2) could then be used to estimate the temperature dependence of the refractive index of the THz wave around the central frequency of 275 GHz. Here, we ignore variation of THz refractive index with frequency in the 253-286.5 GHz range, and the estimated error bar due to this simplification is around ±0.01%, much below our experimental error bars [37].

While calculating the THz refractive index using Eq. 2, one should consider the temperature dependence of lithium niobate's optical group velocity refractive index [38,39]. Here, the growth condition (congruent or stoichiometric) and the MgO doping level of the sample cause slight changes in the reported refractive index values [38–41]. Unfortunately, to our knowledge, the temperature dependence of the refractive index for the pump wavelength has not been studied at cryogenic temperatures yet for LN, and the reported data is for room and elevated temperatures [38–40] . Here, after carefully investigating the reported data in the literature, we have chosen to use the Sellmeier equations provided by Paul et al. in [38] for 5% MgO-doped congruent LN (the slope of variation of group velocity refractive index with temperature is similar to what is reported by Jundt et al. [40] and Edwards et al. [39] for CLN). Using the formula given in [38], we have calculated the group refractive index of 5% MgO CLN in its extraordinary axis as 2.209 at 300 K and as 2.191 at 78 K for a central wavelength of 1030 nm (only a 0.8% decrease with temperature is estimated due to the small thermo-optic coefficient of LN for the near-infrared wavelengths).

While using Eq. 2, one needs to also consider the variation of the QPM period with temperature due to thermal expansion, and for that, we have used the linear thermal expansion data given in [42] for lithium niobate. Here, one can calculate that the QPM period, which is 400 μm at room temperature, shrinks to 399.77 μm at 78 K. The estimated reduction in QPM period length is only 0.06% (although this is rather a quite small change, we have considered this effect also in our analysis for the sake of completeness). One thing to note is that here, we assume that (i) the value for the QPM period given by the manufacturer is correct, and (ii) the variation of the QPM period over the crystal length is also minor.

Fig. 10 summarizes the calculated results for Δn and THz refractive index ($n_{THz}$) for the extraordinary axis of 5% MgO-doped CLN. For comparison with the literature, we have also included the reported values of the THz refractive index for MCLN for different MgO doping levels [30,37] in Fig. 10. One thing to notice is that the pulse-train approach has enabled us to acquire much denser data points compared to earlier reports, which only present results in a few selected temperatures (as the data taking and analysis time is much longer). To our knowledge, the literature lacks MCLN data for 5% MgO doping, but our results are in between what is reported by Pálfalvi et al. [37] and Wu et al. [30] for ~6% MgO-doped CLN samples (there is up to around ±2% difference between our results and the reports of Pálfalvi

et al. and Wu et al. [30,37]). We estimate a THz refractive index of 4.81 at 78 K and 5.09 at 300 K for a central frequency of around 300 GHz.

The most significant error bar in our estimation for THz refractive index calculations is potentially coming from the Sellmeier equations used for the optical group refractive index, and hence, we also report Δn in Fig. 10, which is not affected by this potential error source. We estimate a Δn of 2.62 at 78 K and 2.88 at 300 K for a central frequency of around 275 GHz. For comparison, for higher THz frequencies (~1-2 THz) and for a pump wavelength of around 0.8 μm, Lee et al. reported a Δn of ~2.72 and ~2.91 at 78 and 300 K, respectively, for a PPLN sample [36]. Here, the pump wavelength, the THz frequencies, and the MgO doping of the samples are different, which might be causing the reported difference.

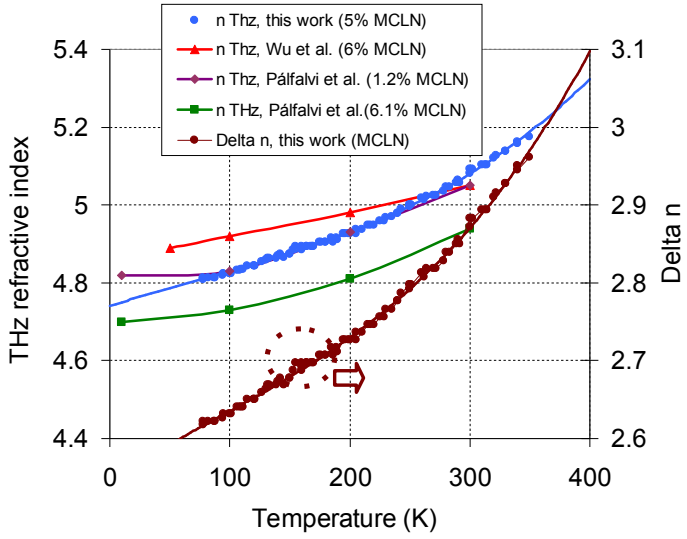


Fig. 10. Calculated variation of THz refractive index with temperature at THz frequencies around 275 GHz. The solid curve is an analytical fit to the measured data (Eq. 3). Comparison with the data in the literature [30,37] is also given. For the sake of completeness, we also plot Δn (the difference between THz refractive index and optical group index for the extraordinary axis of lithium niobate. A 5% MgO-doped congruently grown lithium niobate (MCLN) was used in the experiments.

We provide the following analytical equations that could be used to estimate the temperature variation of THz refractive index and Δn around a center frequency of 275 GHz:

$$n_{THz}(T) = 4.74 + 1\cdot 10^{-3} T - 1.65\cdot 10^{-6} T^2 + 7\cdot 10^{-9} T^3 \qquad (3)$$

$$\Delta n(T) = 2.545 + 1\cdot 10^{-3} T - 1.73\cdot 10^{-6} T^2 + 6.7\cdot 10^{-9} T^3 \qquad (4)$$

Note that, as our temperature-dependent THz data is taken with a large data set, it can also be used to calculate the thermo-optic coefficient (dn/dT) quite accurately (basically via just taking a derivative of Eq. 3):

$$\frac{dn_{THz}}{dT}(T) = 1\cdot 10^{-3} - 3.3\cdot 10^{-6} T + 2.1\cdot 10^{-8} T^2. \qquad (5)$$

Using Eq. 5 we estimate the thermo-optic coefficient for LN near 275 GHz as 0.00087/K and 0.0019/K at 78 K and 300 K, respectively. Our value at room temperature (0.0019/K) is rather close to what has been reported by Sowade et al. (0.0013/K) for a center frequency of 1.4 THz [43]. As the frequency of Sowade et al. is close to the resonance peak of LN around 7.4 THz [13], it is reasonable that our estimate for the thermo-optic coefficient around 300 GHz is smaller than what is reported for 1.4 THz [43].

### *3.3 Temperature dependence of THz efficiency and absorption coefficient in PPLN*

Once the central frequency of operation at different temperatures is determined, as the next step, we took efficiency curves at different temperatures. Fig. 11 shows sample THz efficiency data taken at selected temperatures between 78 and 350 K. For each temperature, the pulse train frequency is adjusted to match the resonance frequency of the PPLN crystal at that temperature (indicated in data captions).

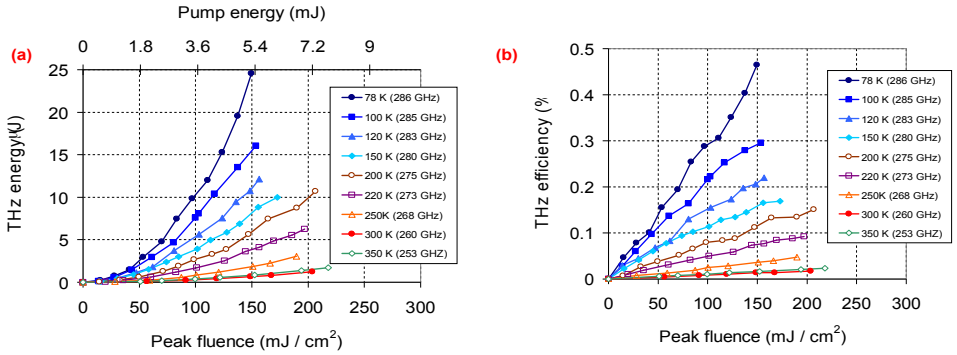


Fig. 11. Measured variation of (a) internal THz energy and (b) internal THz efficiency curves at selected temperatures between 78 K and 350 K. The data is taken using a 3 mm diameter pump beam size and using a pulse train consisting of 64 pulses.

We see from Fig. 11 that, as expected, the THz efficiency increases with decreasing temperature mainly due to the reduction of PPLN material absorption. We have achieved the best performance at 78 K (around 286 GHz), producing an internal THz energy of around 25 μJ at a pump energy of 5.4 mJ. For the 3 mm beam, this corresponds to an internal efficiency of 0.45% at a peak fluence of 150 mJ/cm$^2$. An important point to note here is that we have chosen to stay at the 150 mJ/cm$^2$ fluence level as this enabled us to damage-free operation in the long term (tens of hours). In the short term, it is possible to apply more fluence (maybe safely up to 200-250 mJ/cm$^2$ for a few hours), and in that condition, efficiencies close to 1% could be achieved at the expense of much higher damage risk to the LN crystal. Basically, we have not observed any saturation of THz energy at these fluences, and the limiting factor for efficiency scaling is the relatively low laser-induced damage threshold of lithium niobate at cryogenic temperatures. A fair parameter to compare the results obtained in different studies is then efficiency per fluence. The 0.45% efficiency obtained around 286 GHz at the peak fluence of 150 mJ/cm$^2$ then corresponds to a value of 3 x10$^{-3}$ %/(mJ/cm$^2$), very similar to what we have recently obtained (2.5x10$^{-3}$ %/(mJ/cm$^2$)) around 347 GHz [26].

At room-temperature operation, at the same fluence level of 150 mJ/cm$^2$, the THz energy was as low as 0.7 μJ, corresponding to an internal efficiency of around 0.014%. This corresponds to more than 30 times lower energy at 300 K compared to 78 K: basically, for this 2 cm long crystal, the THz absorption limits the performance quite dramatically at room temperature (room-temperature performance will be better using a short crystal). It is important also to mention that due to the much higher damage threshold of LN material at room temperature, one can safely operate the system at a fluence of 500 mJ/cm$^2$ in the long term and at 1000 mJ/cm$^2$ for the short term (we have observed surface damage in our crystal at a fluence of 1200 mJ/cm$^2$ at room temperature). However, even at a fluence level of 500 mJ/cm$^2$ we have obtained a THz energy of only 3.7 μJ (0.045% efficiency) at room

temperature, which is still 6-7 times lower than cryogenic performance (this high fluence data at room-temperature is taken using a 1.5 mm diameter beam).

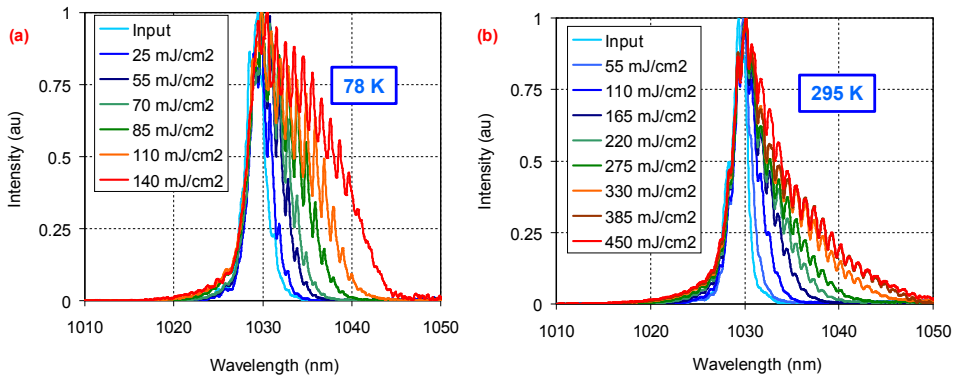


Fig. 12. Measured spectrum of the transmitted pump pulse at different incident peak fluence values at (a) cryogenic (78 K) and (b) room (295 K) temperatures.

To elaborate on this issue a little further, we present the measured spectral shift data of the pump at different peak fluence values both at cryogenic and room temperatures (Fig. 12). In both cases, we have observed a spectral shift towards longer wavelengths due to loss of pump photon energy in the THz generation process. Using the basic energy conservation principle, one can use this spectral shift data to estimate an upper bound for THz conversion efficiency. With that, we have calculated a value of 0.47% at 140 mJ/cm$^2$ at 78 K and a value of 0.44% at 450 mJ/cm$^2$ at room temperature. The efficiency value at cryogenic temperatures is close to what we have estimated for the internal THz generation efficiency (only around 10% above), indicating that at 78 K, the absorption of the lithium niobate crystal should be relatively low (as in good agreement with literature and analysis in the earlier section). On the other hand, for the room-temperature case, the upper bound estimate for internal efficiency from spectral data (0.44%) is way above what we have measured from the system (0.045%). This indicates that most of the generated THz is absorbed within the PPLN crystal at room temperature.

It is also interesting to compare the difference in spectral shapes recorded at different temperatures. The spectral shift data taken at 140 mJ/cm$^2$ peak fluence at 78 K and spectral shift data taken at 450 mJ/cm$^2$ peak fluence at room temperature both indicate an internal efficiency of around 0.4-0.5%. However, the shape of the shifted spectra is quite different in both cases. We see a very homogeneous broadening of the optical spectra at cryogenic temperatures, compared to the asymmetric tail one observes at room temperature. This again shows that only a small portion of the generated THz at initial portions of the PPLN crystal could reach later parts of the crystal at room temperature, and hence the number of photons that can have multiple cascading is rather low, resulting in an asymmetric spectral shift. As a side note, the period of spectral modulation observed in the transmitted spectra agrees with the central frequency of THz generated quite well. At 78 K, a $\Delta\lambda$ of 1.025 nm is measured, which corresponds to a frequency difference of 290 GHz, and at room temperature, a $\Delta\lambda$ of 0.92 nm is observable, which corresponds to a frequency of 260 GHz.

We have further measured the long-term stability of the THz generation process (Fig. 13 (a)). The first 10 minutes of data in Fig. 13 (a) shows shot-to-shot energy fluctuations in the pump laser and THz output. Analyzing the data, we found a shot-to-shot RMS energy stability of 3.95% and 5.99% for the pump and THz energies. The rest of the data in Fig. 13 (a) is then taken with an averaging of 10, to better observe the long-term trends in the data. As we can see, the THz energy is almost constant, and the slow decrease of THz energy observed is due to the slow reduction in pump energy. This clearly shows that a peak fluence of 150

mJ/cm$^2$ is a relatively safe value for the hourly operation of PPLN at cryogenic temperatures (at least for the burst length used here, which was around 200 ps long, and at the repetition rate of 10 Hz). In Fig 13 (b), we show the correlation between pump and THz energy. As we can see, the fluctuations in THz energy are strongly correlated with the pump energy fluctuations, and the Pearson correlation coefficient factor (r) is as high as 0.904. During these measurements, a big part of the setup was not covered, resulting in relatively large fluctuations in pump energy which manifested itself also in THz energy. We believe that in future studies using more stable amplifiers, the shot-to-shot rms noise in THz energy could be reduced below the 1% level [33].

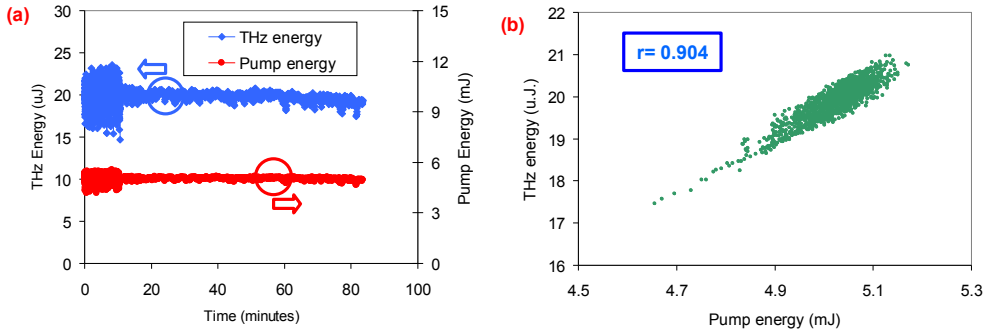


Fig. 13. (a) Measured stability of pump pulse and THz output energies. The first 10 minutes is a shot-to-shot measurement, and after that, an average of 10 is applied to look at the long-term variations. (b) Correlation between pump energy fluctuations and THz energy fluctuations. The Pearson correlation coefficient factor (r) is calculated to be 0.904, indicating a strong positive correlation.

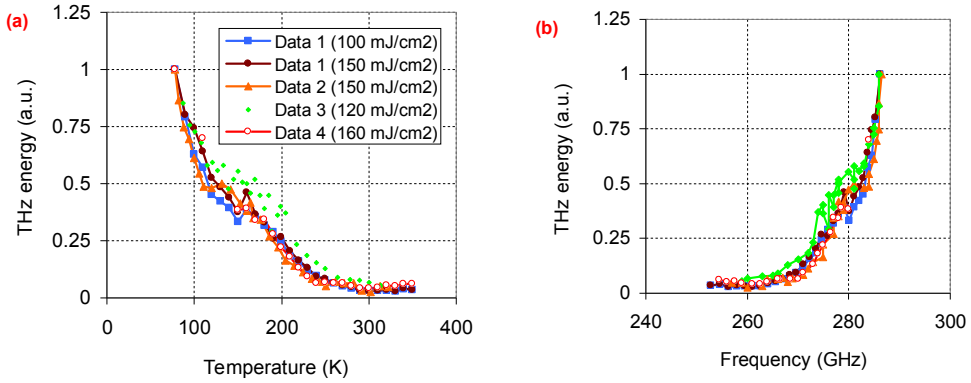


Fig. 14 (a) Measured variation of normalized THz energy with temperature at several different levels of pump peak fluence. (b) Variation of normalized THz energy with THz central frequency upon temperature tuning.

As a final analysis, it is interesting to look at the variation of THz generation efficiency with temperature at fixed fluence values in more detail to try to understand the variation of THz absorption with temperature. For that, Fig. 14 shows the measured variation of THz efficiency with temperature at selected peak fluence values between 100-160 mJ/cm$^2$. Note that the measurement was repeated four times on different days. Some of the data is taken from the frequency scan experiments summarized in the earlier section (e.g., Fig. 9), and the remaining are taken from the data presented in Fig. 11. Undoubtedly, there are some

fluctuations in the data, and the data sets taken in different days differ from each other (up to 10-20% around 150-200 K). On the other hand, one can still use the general trend in the data for some basic observations. From Fig. 14, we see that, first, when the temperature of the PPLN crystal is increased from 78 K to120 K, the THz efficiency drops sharply. Then, between 120 K and ~175 K, we have a plateau-like region where the THz efficiency only decreases slightly with temperature. Later, between 200 K and 300 K, we observe another relatively substantial decrease in efficiency (but indeed not as sharp as the 78-120 K range). Finally, above 300 K, the efficiency is almost constant, and it even increases slightly with temperature (we have repeatedly measured a slightly higher efficiency at 350 K compared to 300 K).

Several groups have reported the variation of THz efficiency with temperature in lithium niobate earlier [7,8,15,16,44,45], and there is quite a significant difference in reported data. The variation of THz generation efficiency with temperature is dependent on many factors, such as the frequency of the THz generated, the method used for THz generation, and the length of the crystal used for THz generation. Hence, a considerable difference between reported data is expected. In general, the trend observed in our work is closest to what is reported in [45] around 1.7 THz using a 7.2 mm length crystal with a QPM period of 60 μm.

The main trend of decrease in THz efficiency with increasing temperature could be explained mainly by the increase of absorption in the PPLN crystal. On top of this, it is relatively well-known that the effective nonlinear optical coefficient, which is proportional to the electro-optic coefficient at these frequencies, is also temperature-dependent [13,27,46] and its value is measured to increase with temperature [47,48] due to the increase of the contribution coming from the ionic nonlinear influence [13]. The experimental results provided by Herzog et al. [47] could be used to model the temperature dependence of the effective nonlinear optical coefficient ($d_{33}$):

$$d_{eff}(T) = d_{eff@295K}\left(0.79 + 2.44 \cdot 10^{-6} T^2\right). \tag{6}$$

In Eq. (6), T is the temperature in Kelvin units and $d_{eff@295K}$ is the effective nonlinear optical coefficient of lithium niobate at room temperature.

To understand the other factors influencing the efficiency via temperature change, one needs to look at the basic analytical formula for estimating THz efficiency. Assuming plane waves and a nondepleted pump, the efficiency of THz generation via optical rectification using a bandwidth-limited ultrashort pulse can be estimated using [4]:

$$\eta_{THz} = g_{bw} \frac{\Omega_0^2 d_{eff}^2 L_{eff}}{\varepsilon_0 c^2 n_{THz} n_{pump}^2 \Delta n} F_{pump}. \tag{7}$$

In Eq. 7, $\varepsilon_0$ is the permittivity of free space, c is the speed of light, $n_{pump}$ is the optical refractive index at the pump wavelength, $\Omega_0$is the central angular frequency of THz at the corresponding resonance, $F_{pump}$ is the pump fluence, and $L_{eff}$ is the effective crystal length. The effective crystal length is reduced due to the absorption, and we have used the following model for an estimation:

$$L_{eff} = \frac{1 - e^{-2\alpha L}}{2\alpha} \tag{8}$$

Note that in Eq (8), L is the crystal length, and α is the THz absorption coefficient (for our case, in the extra-ordinary axis and around a central frequency of 275 GHz). For small absorption values, $L_{eff}$ is equal to the crystal length (L), and for large absorption values it can be approximated by ~1/α.

From Eqs. (7-8), we see that besides absorption and the nonlinear optical coefficient, the temperature dependence of the central frequency of THz ($\Omega_o$, or $2\pi f_o$), the THz refractive index ($n_{THz}$), and the difference between the THz and optical group refractive index (Δn) also influence the THz efficiency. To understand the role of each in our case, in Fig. 15 (a), we show the measured overall efficiency as a function of temperature (red solid curve is an exponential best fit to the measured data, which is shown by red open markers), along with calculated contributions of different factors. We observe that, with increasing temperature, the effective nonlinearity is expected to increase the efficiency, and the remaining factors all tend to decrease the THz efficiency. As a simple first-order analysis, using Eq. (7) and known/measured variation of $n_{THz}$, $\Omega_o$, Δn, $d_{eff}$ and $n_{pump}$, we have tried to isolate the effect of absorption, and the green solid line in Fig. 14 (a) shows the estimated impact of absorption on reducing $L_{eff}$ with increasing temperature. Interestingly, for the case studied, all the other factors almost balance out, and the estimated variation of $L_{eff}$ with the temperature almost follows the measured overall efficiency trend (the red and green solid curves almost overlap with each other).

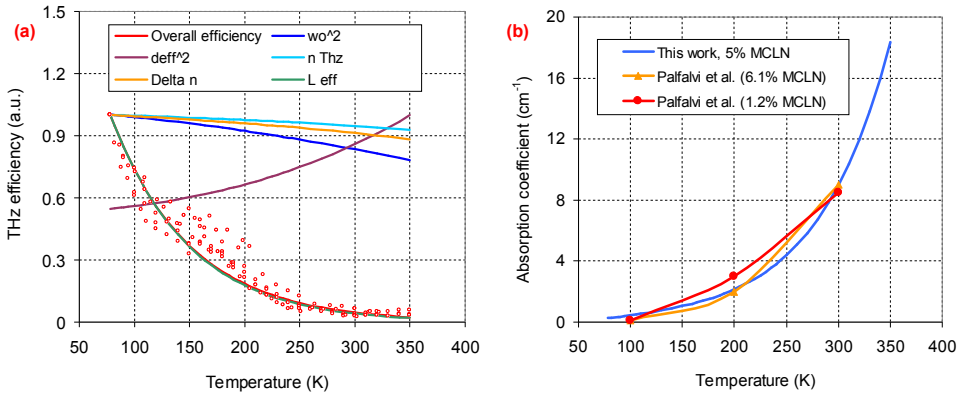


Fig. 15. (a) Measured variation of THz efficiency with PPLN crystal temperature is shown along with the calculated influence of other factors on efficiency such as THz refractive index ($1/n_{THz}$), the square of THz frequency ($f^2$), the square of the effective nonlinear optical coefficient ($d_{eff}^2$), and effective crystal length ($L_{eff}$). (b) Calculated variation of the temperature dependence of the absorption coefficient in lithium niobate near 275 GHz and comparison of the data with the literature [37]. For the Palfalvi et al. results presented in Fig. 15 (b), we used a 2nd order interpolation to estimate the absorption near 275 GHz [37], as the data in [37] do not extend to these low frequencies.

As the second step, using the estimated variation of effective crystal length with temperature, we have tried to estimate the absorption of the LN crystal by using Eq. 8. For that, as a calibration point to our estimation, we have taken the absorption coefficient at room temperature as 9 $cm^{-1}$ [37]. Our absorption coefficient estimate results are shown in Fig. 5 (b). For 5% MCLN, we estimate a THz absorption of around 0.26 $cm^{-1}$ at 78 K, 0.45 $cm^{-1}$ at 100 K, 1.06 $cm^{-1}$ at 150 K, 2.15 $cm^{-1}$ at 200 K, 4.4 $cm^{-1}$ at 250 K and 18.4 $cm^{-1}$ at 350 K for a central frequency of around 275 GHz (assuming an absorption coefficient of 9 $cm^{-1}$ at 300 K [37]). We see that the overall shape of absorption versus temperature is in relatively good agreement with the earlier results presented by Palfavi et al. [37].

Overall, we estimate the absorption coefficient here by making a rough exponential fit to the efficiency data in Fig. 14 (a). Alternative polynomial fits to the same data will result in different absorption estimation curves. Moreover, the method employed for an absorption estimate based on efficiency data has relatively large error bars, as efficiency depends on many factors besides absorption as we discussed earlier. Despite all these issues, there is little THz absorption data for PPLN at these low frequencies in literature, and the absorption data presented here enables an initial insight into this.

## 4. Conclusions

In this work, using a flexible pulse train with adjustable frequency as an excitation source as well as a probing tool [26], we have measured the temperature dependence of frequency response of PPLN crystal near 275 GHz. The method enabled fast and precise determination of the THz refractive index and thermo-optic coefficient in the extraordinary axis of lithium niobate. We have also used the measured variation of THz generation efficiency with temperature to study the temperature dependence of the absorption coefficient of lithium niobate, but here, accurate estimation is more challenging since the THz efficiency depends on many other factors. We have further demonstrated an intrinsic THz conversion efficiency of 0.45% at a safe peak fluence value of 150 mJ/cm$^2$. We believe that the pulse train excitation/ probing approach could become a useful alternative tool for mapping the material properties of nonlinear crystals, especially at low frequencies where other methods, such as THz time-domain spectrometry, have intrinsic difficulty in providing reliable results.


### Funding

Seventh Framework Programme (FP7) FP7/2007- 2013 European Research Council (ERC) Synergy Grant (609920). Deutsche Forschungsgemeinschaft (Project No. 405983224). Deutsches Electronen-Synchrotron (POV-IV – Matter MML-DMC).


### Data Availability

Data underlying the results presented in this paper are not publicly available at this time but may be obtained from the authors upon reasonable request.

### Disclosures

The authors declare no conflicts of interest.

### References


1. A. Leitenstorfer, A. S. Moskalenko, T. Kampfrath, J. Kono, E. Castro-Camus, K. Peng, N. Qureshi, D. Turchinovich, K. Tanaka, A. G. Markelz, M. Havenith, C. Hough, H. J. Joyce, W. J. Padilla, B. Zhou, K.-Y. Kim, X.-C. Zhang, P. U. Jepsen, S. Dhillon, M. Vitiello, E. Linfield, A. G. Davies, M. C. Hoffmann, R. Lewis, M. Tonouchi, P. Klarskov, T. S. Seifert, Y. A. Gerasimenko, D. Mihailovic, R. Huber, J. L. Boland, O. Mitrofanov, P. Dean, B. N. Ellison, P. G. Huggard, S. P. Rea, C. Walker, D. T. Leisawitz, J. R. Gao, C. Li, Q. Chen, G. Valušis, V. P. Wallace, E. Pickwell-MacPherson, X. Shang, J. Hesler, N. Ridler, C. C. Renaud, I. Kallfass, T. Nagatsuma, J. A. Zeitler, D. Arnone, M. B. Johnston, en J. Cunningham, "The 2023 terahertz science and technology roadmap," J. Phys. D. Appl. Phys. **56**(22), 223001 (2023).
2. J.-H. Son, S. J. Oh, en H. Cheon, "Potential clinical applications of terahertz radiation," J. Appl. Phys. **125**(19), 190901 (2019).
3. A. Herter, A. Shams-Ansari, F. F. Settembrini, H. K. Warner, J. Faist, M. Lončar, en I.-C. Benea-Chelmus, "Terahertz waveform synthesis in integrated thin-film lithium niobate platform," Nat. Commun. **14**(1), 11 (2023).
4. K. L. Vodopyanov, "Optical generation of narrow-band terahertz packets in periodically-inverted electro-optic crystals: conversion efficiency and optimal laser pulse format," Opt. Express **14**(6), 2263–2276 (2006).
5. X. Wu, D. Kong, S. Hao, Y. Zeng, X. Yu, B. Zhang, M. Dai, S. Liu, J. Wang, Z. Ren, S. Chen, J. Sang, K. Wang, D. Zhang, Z. Liu, J. Gui, X. Yang, Y. Xu, Y. Leng, Y. Li, L. Song, Y. Tian, en R. Li, "Generation of 13.9-mJ Terahertz Radiation from Lithium Niobate Materials," Adv. Mater. **35**(23), 2208947 (2023).
6. T. Kroh, T. Rohwer, D. Zhang, U. Demirbas, H. Cankaya, M. Hemmer, Y. Hua, L. E. Zapata, M. Pergament, F. X. Kärtner, en N. H. Matlis, "Parameter sensitivities in tilted-pulse-front based terahertz setups and their implications for high-energy terahertz source design and optimization," Opt. Express **30**(14), 24186–24206 (2022).
7. B. Zhang, Z. Ma, J. Ma, X. Wu, C. Ouyang, D. Kong, T. Hong, X. Wang, P. Yang, L. Chen, Y. Li, en J. Zhang, "1.4-mJ High Energy Terahertz Radiation from Lithium Niobates," Laser Photon. Rev. **15**(3), 2000295

(2021).
8. C. Vicario, B. Monoszlai, C. Lombosi, A. Mareczko, A. Courjaud, J. A. Fülöp, en C. P. Hauri, "Pump pulse width and temperature effects in lithium niobate for efficient THz generation," Opt. Lett. **38**(24), 5373–5376 (2013).
9. F. Giorgianni, B. Wehinger, S. Allenspach, N. Colonna, C. Vicario, P. Puphal, E. Pomjakushina, B. Normand, en C. Rüegg, "Ultrafast frustration breaking and magnetophononic driving of singlet excitations in a quantum magnet," Phys. Rev. B **107**(18), 184440 (2023).
10. C. D. W. Mosley, D. S. Lake, D. M. Graham, S. P. Jamison, R. B. Appleby, G. Burt, en M. T. Hibberd, "Large-area periodically-poled lithium niobate wafer stacks optimized for high-energy narrowband terahertz generation," Opt. Express **31**(3), 4041–4054 (2023).
11. H. T. Olgun, W. Tian, G. Cirmi, K. Ravi, C. Rentschler, H. Çankaya, M. Pergament, M. Hemmer, Y. Hua, D. N. Schimpf, N. H. Matlis, en F. X. Kärtner, "Highly efficient generation of narrowband terahertz radiation driven by a two-spectral-line laser in PPLN," Opt. Lett. **47**(10), 2374–2377 (2022).
12. F. Lemery, T. Vinatier, F. Mayet, R. Aßmann, E. Baynard, J. Demailly, U. Dorda, B. Lucas, A.-K. Pandey, en M. Pittman, "Highly scalable multicycle THz production with a homemade periodically poled macrocrystal," Commun. Phys. **3**(1), 150 (2020).
13. D. Jang en K.-Y. Kim, "Multicycle terahertz pulse generation by optical rectification in LiNbO3, LiTaO3, and BBO crystals," Opt. Express **28**(14), 21220–21235 (2020).
14. S. W. Jolly, N. H. Matlis, F. Ahr, V. Leroux, T. Eichner, A.-L. Calendron, H. Ishizuki, T. Taira, F. X. Kärtner, en A. R. Maier, "Spectral phase control of interfering chirped pulses for high-energy narrowband terahertz generation," Nat. Commun. **10**(1), 2591 (2019).
15. F. Ahr, S. W. Jolly, N. H. Matlis, S. Carbajo, T. Kroh, K. Ravi, D. N. Schimpf, J. Schulte, H. Ishizuki, T. Taira, A. R. Maier, en F. X. Kärtner, "Narrowband terahertz generation with chirped-and-delayed laser pulses in periodically poled lithium niobate," Opt. Lett. **42**(11), 2118–2121 (2017).
16. S. Carbajo, J. Schulte, X. Wu, K. Ravi, D. N. Schimpf, en F. X. Kärtner, "Efficient narrowband terahertz generation in cryogenically cooled periodically poled lithium niobate," Opt. Lett. **40**(24), 5762–5765 (2015).
17. K. Uchida, H. Hirori, T. Aoki, C. Wolpert, T. Tamaya, K. Tanaka, T. Mochizuki, C. Kim, M. Yoshita, H. Akiyama, L. N. Pfeiffer, en K. W. West, "Time-resolved observation of coherent excitonic nonlinear response with a table-top narrowband THz pulse wave," Appl. Phys. Lett. **107**(22), 221106 (2015).
18. C. Rentschler, N. H. Matlis, U. Demirbas, Z. Zhang, M. Pergament, A. Zukauskas, C. Canalias, H. Ishizuki, V. Pasiskevicius, F. Laurell, T. Taira, en F. X. Kärtner, "Parameter dependencies in multicycle THz generation with tunable high-energy pulse trains in large-aperture crystals," in *Proc.SPIE* (2024), **12869**, bl 128690M.
19. O. V Chefonov, A. V Ovchinnikov, C. P. Hauri, en M. B. Agranat, "Broadband and narrowband laser-based terahertz source and its application for resonant and non-resonant excitation of antiferromagnetic modes in NiO," Opt. Express **27**(19), 27273–27281 (2019).
20. T. Kubacka, J. A. Johnson, M. C. Hoffmann, C. Vicario, S. de Jong, P. Beaud, S. Grübel, S.-W. Huang, L. Huber, L. Patthey, Y.-D. Chuang, J. J. Turner, G. L. Dakovski, W.-S. Lee, M. P. Minitti, W. Schlotter, R. G. Moore, C. P. Hauri, S. M. Koohpayeh, V. Scagnoli, G. Ingold, S. L. Johnson, en U. Staub, "Large-Amplitude Spin Dynamics Driven by a THz Pulse in Resonance with an Electromagnon," Science (80-. ). **343**(6177), 1333–1336 (2014).
21. X. Su, D. Wang, Q. Tian, Y. Liang, L. Niu, L. Yan, Y. Du, W. Huang, en C. Tang, "Widely tunable narrow-band coherent Terahertz radiation from an undulator at THU," J. Instrum. **13**(01), C01020 (2018).
22. Y.-S. Lee, T. Meade, V. Perlin, H. Winful, T. B. Norris, en A. Galvanauskas, "Generation of narrow-band terahertz radiation via optical rectification of femtosecond pulses in periodically poled lithium niobate," Appl. Phys. Lett. **76**(18), 2505–2507 (2000).
23. C. Zhang, Y. Avetisyan, G. Abgaryan, I. Kawayama, H. Murakami, en M. Tonouchi, "Tunable narrowband terahertz generation in lithium niobate crystals using a binary phase mask," Opt. Lett. **38**(6), 953–955 (2013).
24. A. G. Stepanov, J. Hebling, en J. Kuhl, "Generation, tuning, and shaping of narrow-band, picosecond THz pulses by two-beam excitation," Opt. Express **12**(19), 4650–4658 (2004).
25. J. Ahn, A. V Efimov, R. D. Averitt, en A. J. Taylor, "Terahertz waveform synthesis via optical rectification of shaped ultrafast laser pulses," Opt. Express **11**(20), 2486–2496 (2003).
26. N. H. Matlis, Z. Zhang, U. Demirbas, C. Rentschler, K. Ravi, M. Youssef, G. Cirmi, M. Pergament, M. Edelmann, S. M. Mohamadi, S. Reuter, en  and F. X. Kärtner, "Precise parameter control of multicycle terahertz generation in PPLN using flexible pump pulse trains," Opt. Express **31**(26), 44424–44443 (2023).
27. A. Buzády, R. Gálos, G. Makkai, X. Wu, G. Tóth, L. Kovács, G. Almási, J. Hebling, en L. Pálfalvi, "Temperature-dependent terahertz time-domain spectroscopy study of Mg-doped stoichiometric lithium niobate," Opt. Mater. Express **10**(4), 998–1006 (2020).
28. V. D. Antsygin, A. A. Mamrashev, L. V Maximov, S. L. Mikerin, F. A. Minakov, en N. A. Nikolaev, "Temperature Dependence of Terahertz Properties of Stoichiometric Lithium Tantalate," J. Infrared, Millimeter, Terahertz Waves **43**(11), 895–904 (2022).

29. K. A. Kuznetsov, G. K. Kitaeva, S. P. Kovalev, S. A. Germansky, A. M. Buryakov, A. N. Tuchak, en A. N. Penin, "Complex extraordinary dielectric function of Mg-doped lithium niobate crystals at terahertz frequencies," Appl. Phys. B **122**(8), 223 (2016).
30. X. Wu, C. Zhou, W. R. Huang, F. Ahr, en F. X. Kärtner, "Temperature dependent refractive index and absorption coefficient of congruent lithium niobate crystals in the terahertz range," Opt. Express **23**(23), 29729–29737 (2015).
31. A. L. Calendron, H. Cankaya, en F. X. Kartner, "High-energy kHz Yb:KYW dual-crystal regenerative amplifier," Opt. Express **22**(20), 24752–24762 (2014).
32. M. Pergament, M. Kellert, U. Demirbas, J. Thesinga, S. Reuter, Y. Liu, Y. Hua, M. Kilinc, A. Yakovlev, en F. X. Kärtner, "100-mJ, 100-W cryogenically cooled Yb:YLF laser," Opt. Lett. **48**(11), 2833–2836 (2023).
33. U. Demirbas, M. Kellert, J. Thesinga, Y. Hua, S. Reuter, M. Pergament, en F. X. Kärtner, "Highly efficient cryogenic Yb:YLF regenerative amplifier with 250 W average power," Opt. Lett. **46**(16), 3865–3868 (2021).
34. U. Demirbas, C. Rentschler, Z. Zhang, M. Pergament, N. H. Matlis, en F. X. Kärtner, "Two-dimensional effects in Multicycle THz generation with tunable pump pulse trains in lithium niobate," in *2023 48th International Conference on Infrared, Millimeter, and Terahertz Waves (IRMMW-THz)* (2023), bll 1–2.
35. T. Kroh, T. Rohwer, L. Wang, U. Demirbas, H. Cankaya, M. Pergament, F. X. Kärtner, en N. H. Matlis, "Robust optimization of single-cycle THz setups based on phase-matching via tilted pulse fronts using an incident-fluence metric," **11264**(2), 1126416 (2020).
36. Y. S. Lee, T. Meade, T. B. Norris, en A. Galvanauskas, "Tunable narrow-band terahertz generation from periodically poled lithium niobate," Appl. Phys. Lett. **78**(23), 3583–3585 (2001).
37. L. Pálfalvi, J. Hebling, J. Kuhl, Á. Péter, en K. Polgár, "Temperature dependence of the absorption and refraction of Mg-doped congruent and stoichiometric LiNbO3 in the THz range," J. Appl. Phys. **97**(12), 123505 (2005).
38. O. Paul, A. Quosig, T. Bauer, M. Nittmann, J. Bartschke, G. Anstett, en J. A. L'huillier, "Temperature-dependent Sellmeier equation in the MIR for the extraordinary refractive index of 5% MgO doped congruent LiNbO3," Appl. Phys. B **86**(1), 111–115 (2007).
39. G. J. Edwards en M. Lawrence, "A temperature-dependent dispersion equation for congruently grown lithium niobate," Opt. Quantum Electron. **16**(4), 373–375 (1984).
40. D. H. Jundt, "Temperature-dependent Sellmeier equation for the index of refraction, ne, in congruent lithium niobate," Opt. Lett. **22**(20), (1997).
41. O. Gayer, Z. Sacks, E. galun, en A. Arie, "Temperature and wavelength dependent refractive index equations for MgO-doped congruent and stoichiometric LiNbO3," Appl. Phys. B **91**, 343–348 (2008).
42. J. S. Browder en S. S. Ballard, "Thermal expansion data for eight optical materials from 60 K to 300 K," Appl. Opt. **16**(12), 3214–3217 (1977).
43. R. Sowade, I. Breunig, C. Tulea, en K. Buse, "Nonlinear coefficient and temperature dependence of the refractive index of lithium niobate crystals in the terahertz regime," Appl. Phys. B **99**(1), 63–66 (2010).
44. S.-W. Huang, E. Granados, W. R. Huang, K.-H. Hong, L. E. Zapata, en F. X. Kärtner, "High conversion efficiency, high energy terahertz pulses by optical rectification in cryogenically cooled lithium niobate," Opt. Lett. **38**(5), 796–798 (2013).
45. Y.-S. Lee, T. Meade, M. DeCamp, T. B. Norris, en A. Galvanauskas, "Temperature dependence of narrow-band terahertz generation from periodically poled lithium niobate," Appl. Phys. Lett. **77**(9), 1244–1246 (2000).
46. Y. Liu, G. Ren, T. Cao, R. Mishra, en J. Ravichandran, "Modeling temperature, frequency, and strain effects on the linear electro-optic coefficients of ferroelectric oxides," J. Appl. Phys. **131**(16), 163101 (2022).
47. C. Herzog, G. Poberaj, en P. Günter, "Electro-optic behavior of lithium niobate at cryogenic temperatures," Opt. Commun. **281**(4), 793–796 (2008).
48. P. Górski, R. Ledzion, K. Bondarczuk, en W. Kucharczyk, "Temperature dependence of linear electrooptic coefficients r113 and r333 in lithium niobate," Opto-Electronics Rev. **16**(1), 46–48 (2008).